

Electronic Supplementary Information

Samarium Activated $\text{La}_2\text{Hf}_2\text{O}_7$ Nanoparticles as Multifunctional Phosphors

Santosh K. Gupta^{1,2}, Maya Abdou¹, Jose P. Zuniga¹, Alexander A. Puretzky³, and Yuanbing Mao^{1,4,5*}

¹Department of Chemistry, University of Texas Rio Grande Valley, 1201 West University Drive, Edinburg, Texas 78539, USA

²Radiochemistry Division, Bhabha Atomic Research Centre, Trombay, Mumbai 400085, India

³Center for Nanophase Materials Sciences, Oak Ridge National Laboratory, Oak Ridge, TN 37831, USA

⁴School of Earth, Environmental, and Marine Sciences, University of Texas Rio Grande Valley, 1201 West University Drive, Edinburg, Texas 78539, USA

⁵Current address: Department of Chemistry, Illinois Institute of Technology, 3105 South Dearborn Street, Chicago, IL 60616, USA

*To whom correspondence should be addressed. E-mail: ymao17@iit.edu, Tel.: +1-312-567-3815.

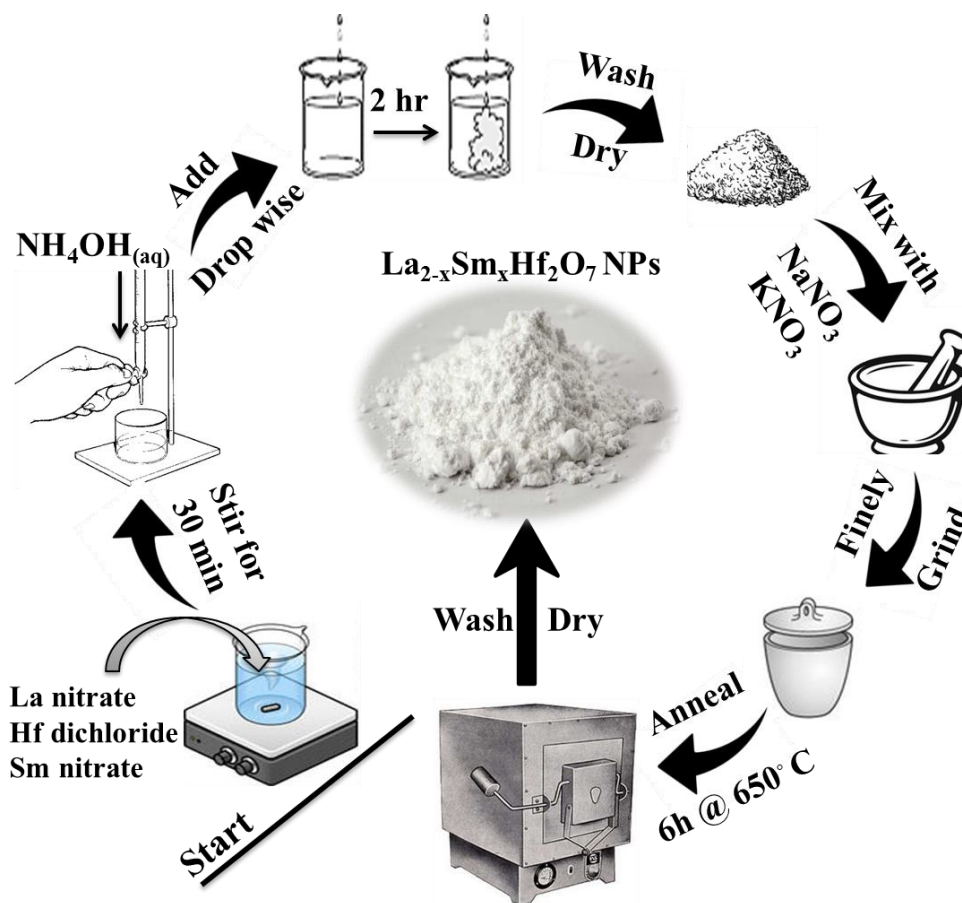


Figure S1. Hybrid coprecipitation and MSS synthesis process of the LHOS NPs.

Characterization Results of the LHOS NPs

Phase analysis

XRD patterns of the LHOS NPs with different Sm^{3+} concentrations (Figure S2a) can be indexed to single phase pyrochlore $\text{La}_2\text{Hf}_2\text{O}_7$ (JCPDS# 37-1040) with the peaks at 28° , 33° , 48° , and 56° corresponding to the (222), (400), (440), and (622) planes. The sharp diffraction peaks demonstrate that the LHOS NPs are highly crystalline. The diffraction peaks of the LHOS NPs exhibit right-hand shifting to higher 2-theta angle as the Sm^{3+} doping concentration increases because the ionic radius of 8-coordinated Sm^{3+} ($r = 1.079 \text{ \AA}$) is smaller than that of 8-coordinated La^{3+} ($r = 1.160 \text{ \AA}$). This phenomenon can be visualized from the magnified (622) reflection peaks shown in Figure S2b. Correspondingly, the lattice constant value reduces slightly with increasing Sm^{3+} doping concentration (Table S1), which can be attributed to smaller Sm^{3+} ions residing at the La^{3+} sites. The crystallite size of the LHOS NPs is calculated using the Debye-Scherrer equation (1):

$$d = K\lambda/B\cos\theta \quad (1)$$

where d is the crystallite size for a given (hkl) reflection, K is the Scherrer constant known as shape factor and is usually taken as 0.89 for spherical particles, λ is the wavelength of Cu K α X-ray radiation (1.5406 Å), B is the full width half maxima (FWHM) value in radians for the peak under consideration, and θ is the peak position for the corresponding (hkl) reflection. The calculated average crystallite size of the LHOS NPs (Table S1) decreases with increasing Sm³⁺ concentration.

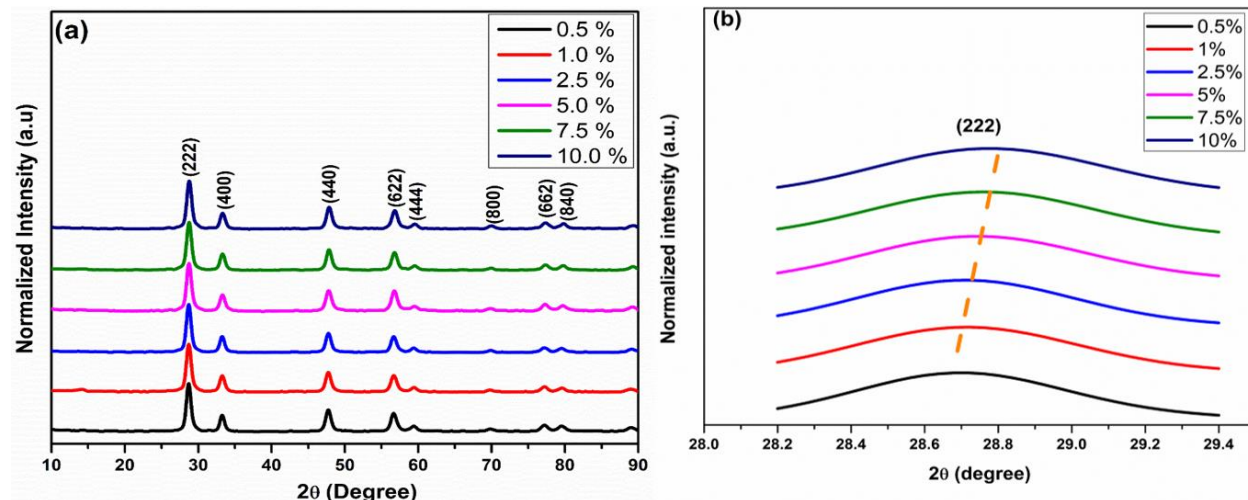


Figure S2. (a) XRD patterns and (b) the shifting of the (622) peak with Sm³⁺ doping concentration of the LHOS NPs.

Table S1. Lattice parameter and calculated crystallite size of the LHOS NPs

[Sm ³⁺] (mol%)	2θ (°)	FWHM (β)	Lattice parameter (Å)	Crystallite size from XRD (nm)	Particle size from SEM (nm)
0.5	28.71	0.281	10.762	28.27 ± 0.5	70.04 ± 1.7
1.0	28.72	0.304	10.759	26.13 ± 0.5	39.22 ± 0.9
2.5	28.73	0.326	10.755	24.37 ± 0.5	35.74 ± 1.1
5.0	28.74	0.353	10.751	22.51 ± 0.5	32.33 ± 1.1
7.5	28.81	0.361	10.726	22.01 ± 0.5	30.40 ± 0.7
10	28.84	0.364	10.715	21.83 ± 0.5	21.94 ± 0.6

Morphological analysis: Scanning electron microscopy

SEM images of the LHOS NPs (Figure S3a-f) show that their mean diameters are in the range of 25-70 nm. The particle size distribution of the LHOS NPs was calculated from these SEM images by ImageJ software and shown in the insets of Figure S4. The LHOS NPs are spherical particles with narrow size distribution and slight agglomeration. Average particle size is estimated from the SEM images whereas crystallite size is calculated from the XRD data. Crystallite size could be different from particle size in case of agglomerated and/or polycrystalline samples. That is why we saw differences from our SEM and XRD data. It is reported that nanospheres exhibit the best emission performance due to their lower scattering loss, therefore increases the screen brightness of display, as consistent with our PL data below.¹⁴

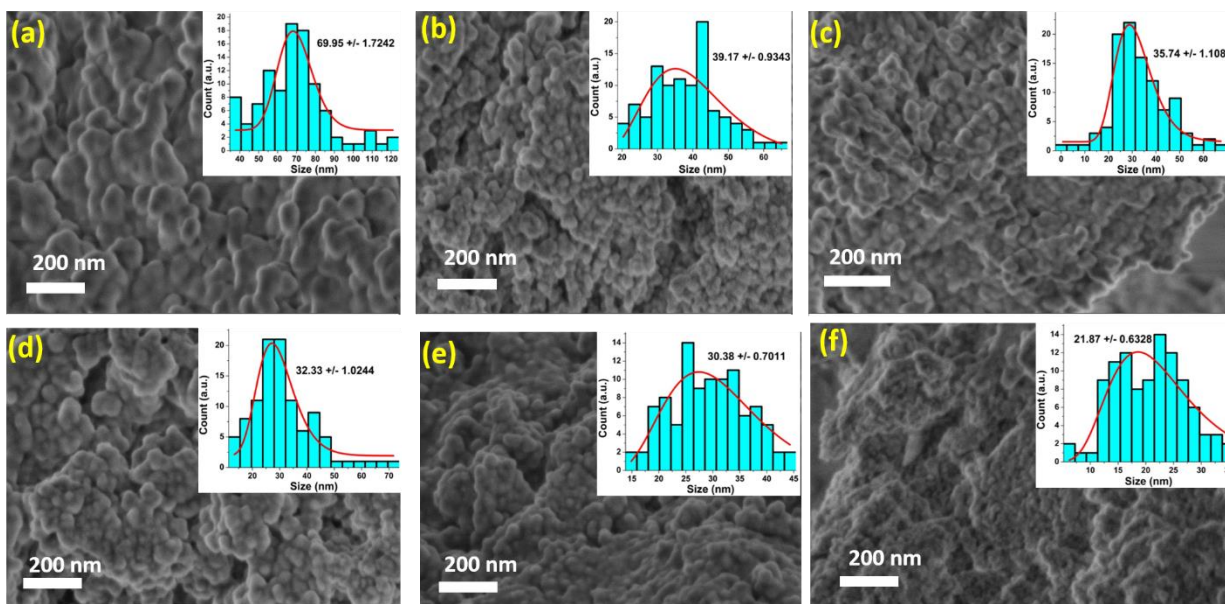


Figure S3. SEM images of the LHOS NPs with different Sm^{3+} doping concentrations: (a) 0.5%, (b) 1.0%, (c) 2.5%, (d) 5.0%, (e) 7.5%, and (f) 10.0%.

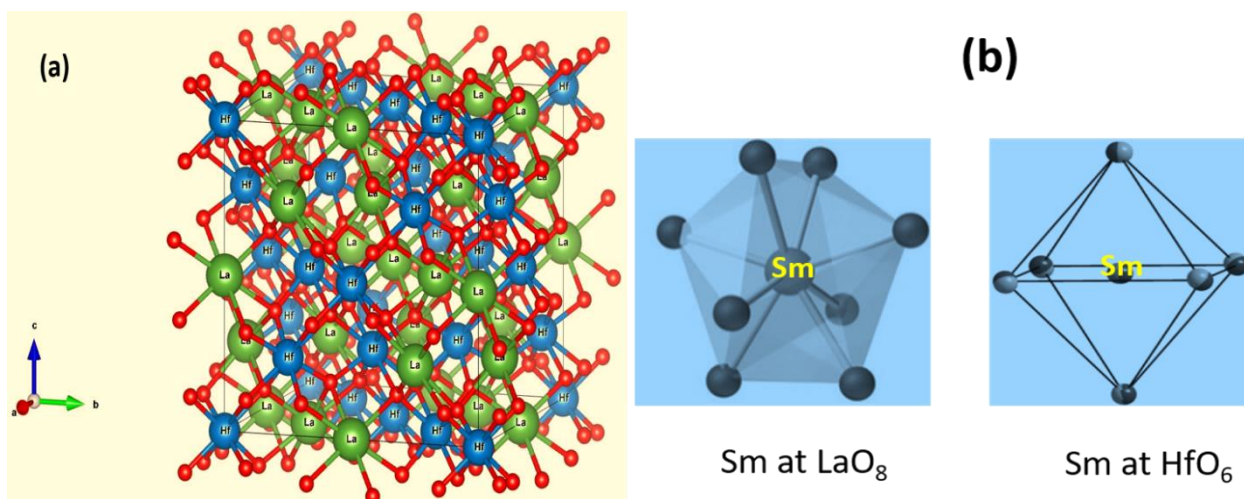


Figure S4. (a) Crystal structure of $\text{La}_2\text{Hf}_2\text{O}_7$ and (b) Sm ion occupying LaO_8 scalenohedra and HfO_6 octahedra.

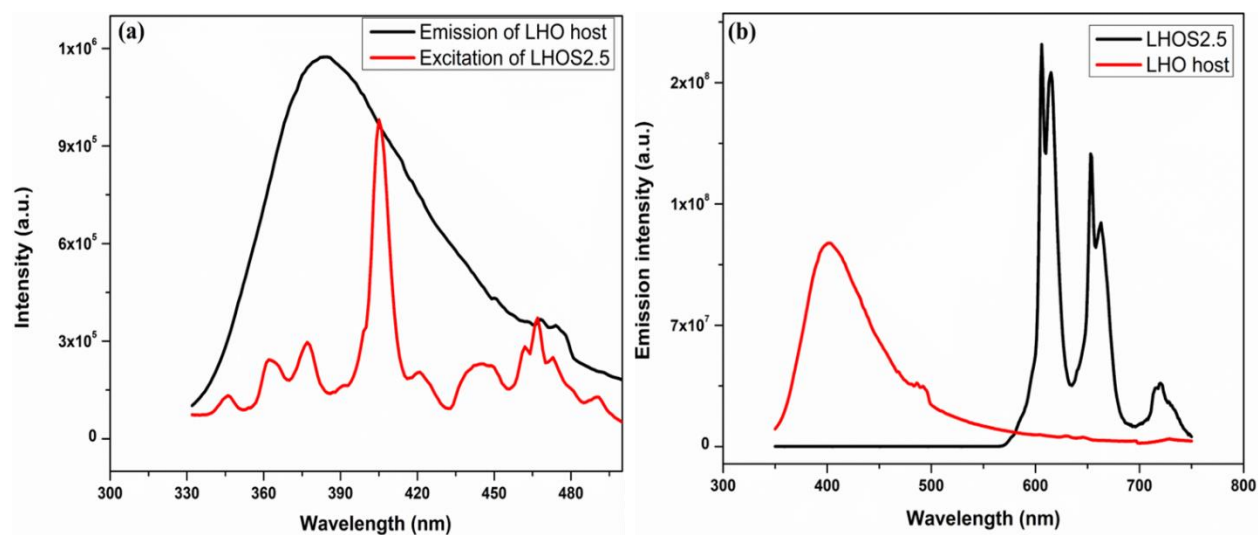


Figure S5. (a) Emission spectrum of the LHO host and excitation spectrum of the LHOS NPs. (b) Corresponding spectra to show the energy transfer from the LHO host to Sm^{3+} ion in the LHOS NPs after vacuum sintering.

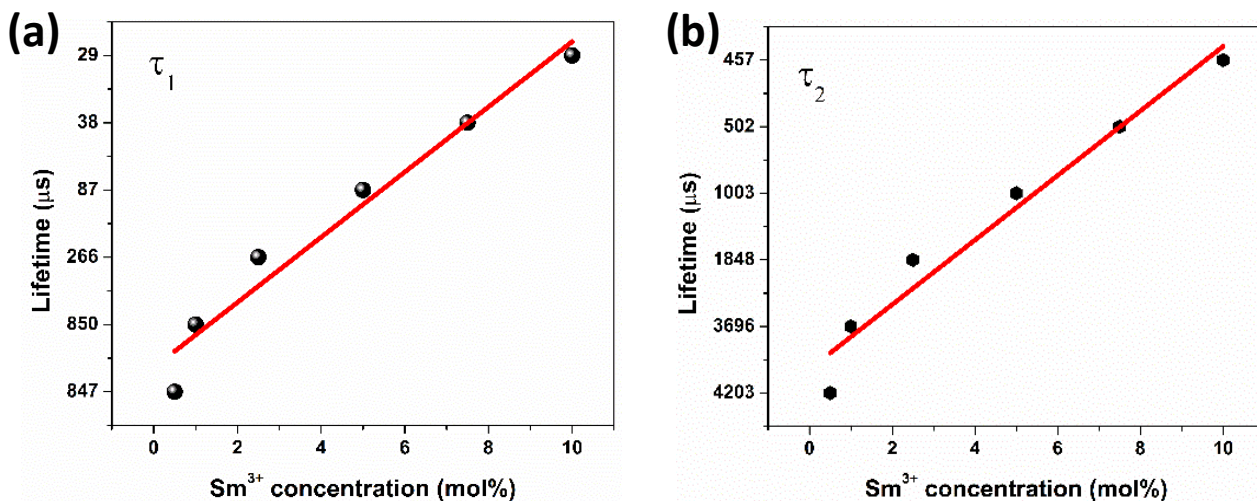


Figure S6. (a) Short- and (b) long-lived lifetimes as a function of Sm^{3+} concentration.

Table S2. Concentration quenching values for various Sm^{3+} doped phosphors

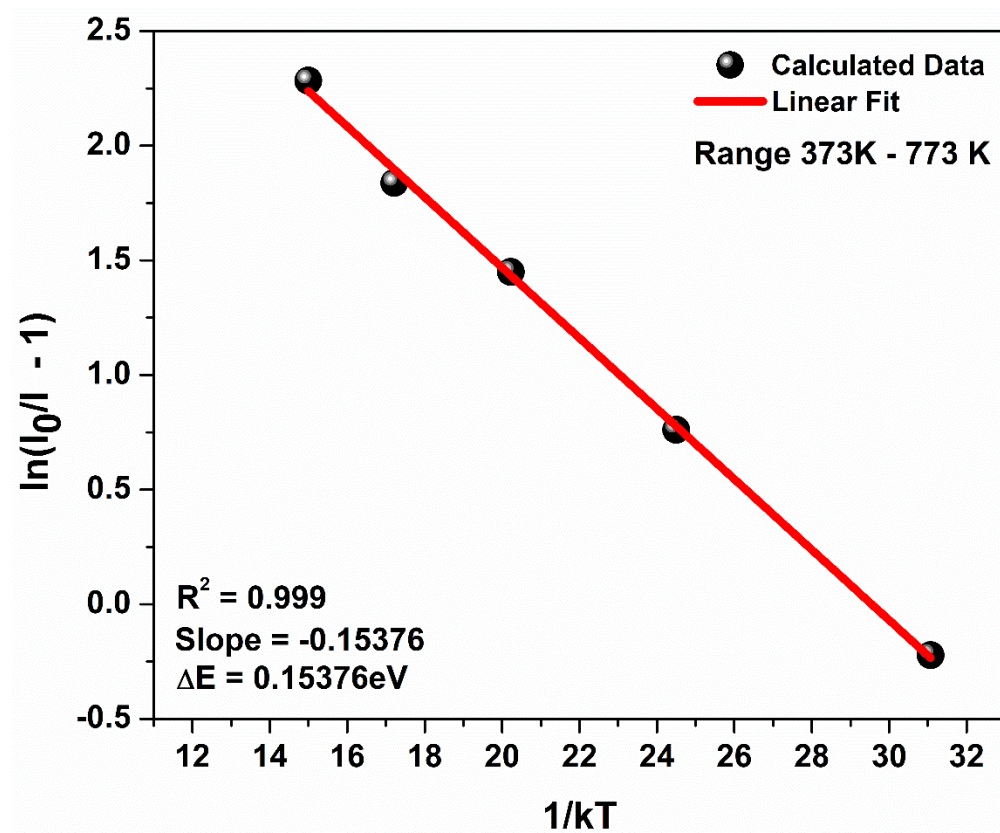
Sm^{3+} doping phosphors	Concentration quenching values (mol%)
CaAl_4O_7	2.0^{15}
$\text{LaAlGe}_2\text{O}_7$	3.0^{16}
$\text{Y}_2\text{O}_2\text{S}$	3.0^{17}
BaMoO_4	8.0^{18}
$\text{Gd}_2\text{Zr}_2\text{O}_7$	3.5^{19}
$\text{Zn}_2\text{P}_2\text{O}_7$	1.0^{20}
$\text{Nd}_2\text{Zr}_2\text{O}_7$	3.0^{21}

Table S3. Luminescence lifetimes of the LHOS NPs

Sm^{3+} doping level (mol %)	τ_1 (μs)	τ_2 (μs)
0.5	847 ± 23	4203 ± 10
1.0	850 ± 20	3696 ± 9
2.5	266 ± 19	1848 ± 7
5.0	87 ± 20	1003 ± 5
7.5	38 ± 15	502 ± 4
10.0	29 ± 15	457 ± 4

Table S4. CIE and CCT values of the LHOS NPs under 405 nm excitation

Sm ³⁺ doping level (mol %)	x	y	CCT (K)
0.5	0.666135	0.33608	3266
1	0.666324	0.33342	3378
2.5	0.667296	0.33245	3437
5	0.665533	0.33421	3331
7.5	0.661982	0.33774	3129
10	0.660624	0.33909	3057

**Figure S7.** Plot of $\ln(I_0/I - 1)$ vs. $1/kT$ of the LHOS (2.5 %) NPs.

To study the high temperature structure stability of the LHOS NPs, we performed in-situ XRD and Raman spectroscopy measurements (Figure S8a and S8b, respectively). It can be seen that the LHOS NPs do not undergo any structural change from room temperature to 900°C and remain in ideal pyrochlore structure. Thermal and structural stability has a profound influence in designing

high temperature phosphors for applications in phosphor converted light emitting diodes, plasma display panels and thermographic sensors.¹¹⁻¹³

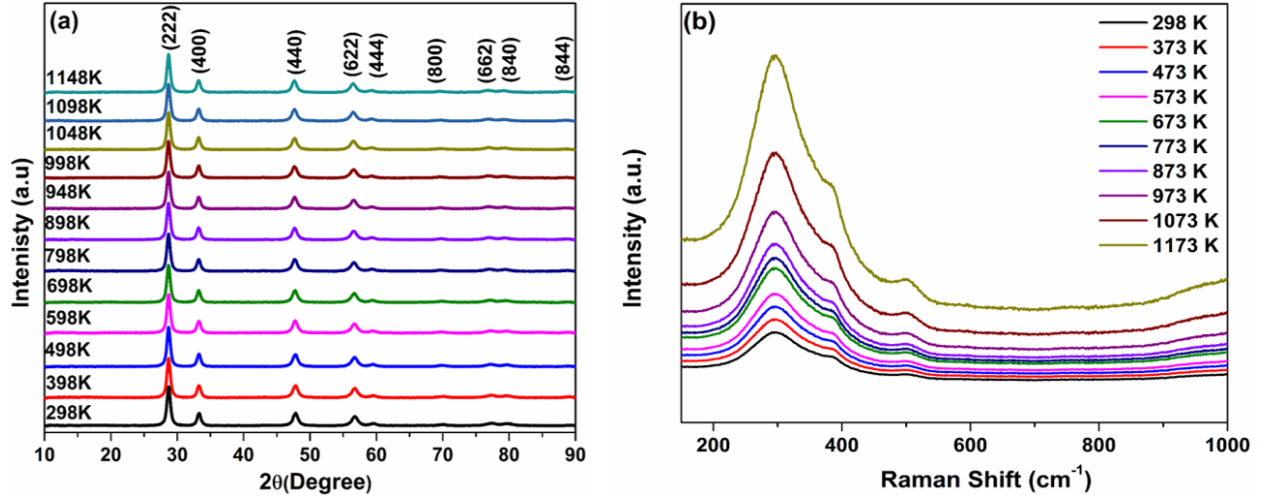


Figure S8. (a) In situ XRD and (b) in situ Raman spectra of the LHOS NPs (2.5mol% Sm³⁺).

Equations used in the main text:

$$R_c = 2\left(\frac{3V}{4\pi X_c N}\right)^{\frac{1}{3}} \quad (S1)$$

where R_c is the distance between donor (dopant) and acceptor (quenching site) which is approximately equal to twice of the radius of a sphere with the volume V , N is the number of Z ions per unit cell, V is the unit cell volume, and X_c is the critical concentration (0.025 in our case here).

$$I/x = K[1 + \beta(x)\theta/3]^{-1} \quad (S2)$$

where x is the dopant concentration which is not less than the critical concentration X_c , I/x is the emission intensity I per activator concentration x , K and β are constants for a given phosphor under the same excitation condition, and the θ value indicates the type of electric multipolar character responsible for concentration quenching.

$$\log(I/x) = K' - (\theta/3)\log x \quad (S3)$$

where $K' = \log K - \log \beta$.

$$I = I_0 + B_1 \exp(-t/\tau_1) + B_2 \exp(-t/\tau_2) \quad (S4)$$

where I_0 is the initial emission intensity at time $t = 0$, and τ_1 and τ_2 are the short and long lifetime values.

$$CCT(x, y) = -449n^3 + 3525n^2 - 6823.3n + 5520.33 \quad (S5)$$

where $n = (x - x_e)/(y - y_e)$ is the inverse slope line, ($x_e = 0.3320$, $y_e = 0.1858$) is the “epicenter” which is close to the intersection point mentioned by Kelly.

$$I(T) = A * e^{\frac{-\Delta E}{K_B * T}} \quad (S6)$$

where $I(T)$ corresponds to the integrated PL intensity at temperature T , K_B is Boltzmann constant whose value is $0.69503 \text{ cm}^{-1} \cdot \text{K}^{-1}$, and A is a pre-exponential factor whose value is 0.29.

$$\ln\left(\frac{I_0}{I} - 1\right) = \ln A - \frac{\Delta E}{kT} + C \quad (S7)$$

whereas I_0 expresses the initial PL intensity, I the PL emission intensity at a given temperature T , ΔE denotes the activation energy involved, and k is the Boltzmann constant.

$$S_a = C * e^{\left(\frac{-\Delta E}{K_B T}\right)} * e^{\left(\frac{\Delta E}{K_B T^2}\right)} \quad (S8)$$

where ΔE is the energy gap between Sm^{3+} successive energy levels, K_B is Boltzmann constant, and T is absolute temperature.

$$S_r = \frac{1}{I} \frac{dI}{dT} \frac{C * e^{\left(\frac{-\Delta E}{K_B T}\right)}}{B + C * e^{\left(\frac{-\Delta E}{K_B T}\right)}} * e^{\left(\frac{\Delta E}{K_B T^2}\right)} * 100\% \quad (S9)$$

References:

1. Sayed, F. N.; Grover, V.; Bhattacharyya, K.; Jain, D.; Arya, A.; Pillai, C.; Tyagi, A., $\text{Sm}_{2-x}\text{Dy}_x\text{Zr}_2\text{O}_7$ pyrochlores: probing order– disorder dynamics and multifunctionality. *Inorg. Chem.* **2011**, *50*, 2354-2365.
2. Turner, K. M.; Rittman, D. R.; Heymach, R. A.; Tracy, C. L.; Turner, M. L.; Fuentes, A. F.; Mao, W. L.; Ewing, R. C., Pressure-induced structural modifications of rare-earth hafnate pyrochlore. *J. Phys.: Condens. Matter* **2017**, *29*, 255401.
3. Subramanian, M.; Aravamudan, G.; Rao, G. S., Oxide pyrochlores—a review. *Prog. Solid State Chem.* **1983**, *15*, 55-143.
4. Zuniga, J. P.; Gupta, S. K.; Abdou, M.; Mao, Y., Effect of molten salt synthesis processing duration on the photo- and radioluminescence of UV-, Visible-, and X-ray-excitable $\text{La}_2\text{Hf}_2\text{O}_7:\text{Eu}^{3+}$ nanoparticles. *ACS Omega* **2018**, *3*, 7757-7770.

5. Pokhrel, M.; Gupta, S. K.; Wahid, K.; Mao, Y., Pyrochlore Rare-Earth Hafnate $\text{RE}_2\text{Hf}_2\text{O}_7$ (RE = La and Pr) Nanoparticles Stabilized by Molten-Salt Synthesis at Low Temperature. *Inorganic Chemistry* **2019**.
6. Garg, N.; Pandey, K. K.; Murli, C.; Shanavas, K. V.; Mandal, B. P.; Tyagi, A. K.; Sharma, S. M., Decomposition of lanthanum hafnate at high pressures. *Phys. Rev. B* **2008**, *77*, 214105.
7. Zinatloo-Ajabshir, S.; Salavati-Niasari, M., Facile synthesis of nanocrystalline neodymium zirconate for highly efficient photodegradation of organic dyes. *Journal of Molecular Liquids* **2017**, *243*, 219-226.
8. Gupta, S. K.; Zuniga, J. P.; Abdou, M.; Mao, Y., Thermal annealing effects on $\text{La}_2\text{Hf}_2\text{O}_7:\text{Eu}^{3+}$ nanoparticles: A curious case study of structural evolution and site-specific photo- and radio-luminescence. *Inorganic Chemistry Frontiers* **2018**, *5*, 2508-2521.
9. Sevastyanov, V. G.; Simonenko, E. P.; Simonenko, N. P.; Stolyarova, V. L.; Lopatin, S. I.; Kuznetsov, N. T., Synthesis, vaporization and thermodynamic properties of superfine $\text{Nd}_2\text{Hf}_2\text{O}_7$ and $\text{Gd}_2\text{Hf}_2\text{O}_7$. *European Journal of Inorganic Chemistry* **2013**, *2013*, 4636-4644.
10. Klee, W. E.; Weitz, G., Infrared spectra of ordered and disordered pyrochlore-type compounds in the series $\text{RE}_2\text{Ti}_2\text{O}_7$, $\text{RE}_2\text{Zr}_2\text{O}_7$ and $\text{RE}_2\text{Hf}_2\text{O}_7$. *Journal of Inorganic and Nuclear Chemistry* **1969**, *31* (8), 2367-2372.
11. Tian, Y., Development of phosphors with high thermal stability and efficiency for phosphor-converted LEDs. *Journal of Solid State Lighting* **2014**, *1* (1), 11.
12. Im, W. B.; Kim, Y.-I.; Jeon, D. Y., Thermal Stability Study of $\text{BaAl}_2\text{Si}_2\text{O}_8:\text{Eu}^{2+}$ Phosphor Using Its Polymorphism for Plasma Display Panel Application. *Chemistry of Materials* **2006**, *18* (5), 1190-1195.
13. Khalid, A. H.; Kontis, K., Thermographic Phosphors for High Temperature Measurements: Principles, Current State of the Art and Recent Applications. *Sensors (Basel, Switzerland)* **2008**, *8* (9), 5673-5744.
14. Sivakami, R.; Thiyagarajan, P., Synthesis and luminescence properties of $\text{ZnS}:\text{Ce}^{3+}, \text{Li}^+, \text{Mn}^{2+}$ nanophosphors. *Nano-Structures & Nano-Objects* **2016**, *6*, 59-66.
15. Puchalska, M.; Zych, E., The effect of charge compensation by means of Na^+ ions on the luminescence behavior of Sm^{3+} -doped CaAl_4O_7 phosphor. *Journal of Luminescence* **2012**, *132*, 826-831.
16. Li, Y.-C.; Chang, Y.-H.; Lin, Y.-F.; Chang, Y.-S.; Lin, Y.-J., Synthesis and luminescent properties of Ln^{3+} (Eu^{3+} , Sm^{3+} , Dy^{3+})-doped lanthanum aluminum germanate $\text{LaAlGe}_2\text{O}_7$ phosphors. *Journal of Alloys and Compounds* **2007**, *439*, 367-375.
17. Lei, B.; Liu, Y.; Tang, G.; Ye, Z.; Shi, C., Spectra and long-lasting properties of Sm^{3+} -doped yttrium oxysulfide phosphor. *Materials Chemistry and Physics* **2004**, *87*, 227-232.
18. Xia, Z.; Chen, D., Synthesis and Luminescence Properties of $\text{BaMoO}_4:\text{Sm}^{3+}$ Phosphors. *Journal of the American Ceramic Society* **2010**, *93*, 1397-1401.
19. Gupta, S. K.; Reghukumar, C.; Sudarshan, K.; Ghosh, P. S.; Pathak, N.; Kadam, R. M., Orange-red emitting $\text{Gd}_2\text{Zr}_2\text{O}_7:\text{Sm}^{3+}$: Structure-property correlation, optical properties and defect spectroscopy. *Journal of Physics and Chemistry of Solids* **2018**, *116*, 360-366.
20. Gupta, S. K.; Pathak, N.; Sahu, M.; Natarajan, V., A Novel near white light emitting nanocrystalline $\text{Zn}_2\text{P}_2\text{O}_7:\text{Sm}^{3+}$ derived using citrate precursor route: Photoluminescence spectroscopy. *Advanced Powder Technology* **2014**, *25*, 1388-1393.
21. Gupta, S. K.; Reghukumar, C.; Kadam, R. M., Eu^{3+} local site analysis and emission characteristics of novel $\text{Nd}_2\text{Zr}_2\text{O}_7:\text{Eu}$ phosphor: insight into the effect of europium concentration on its photoluminescence properties. *RSC Advances* **2016**, *6*, 53614-53624.